



Research Article

Open Access



# Micro-electromechanical system-based cryogenic and heating *in situ* transmission electron microscopy for investigating phase transitions and domain evolution in single-crystal BaTiO<sub>3</sub>

Tianshu Jiang<sup>1</sup> , Yevheniy Pivak<sup>2</sup>, Fan Ni<sup>3</sup>, Gijs van der Gugten<sup>2</sup>, Junjie Li<sup>4</sup>, Fangping Zhuo<sup>3</sup> , Leopoldo Molina-Luna<sup>1</sup> 

<sup>1</sup>Advanced Electron Microscopy Division, Department of Materials and Earth Sciences, Technical University of Darmstadt, Darmstadt 64287, Germany.

<sup>2</sup>DENSolutions BV, Delft 2628, the Netherlands.

<sup>3</sup>Nonmetallic-Inorganic Materials Division, Department of Materials and Earth Sciences, Technical University of Darmstadt, Darmstadt 64287, Germany.

<sup>4</sup>Sichuan Province Key Laboratory of Information Materials and Devices Application, College of Optoelectronic Engineering, Chengdu University of Information Technology, Chengdu 610225, Sichuan, China.

**Correspondence to:** Dr. Fangping Zhuo, Nonmetallic-Inorganic Materials Division, Department of Materials and Earth Sciences, Technical University of Darmstadt, Peter-Grünberg-Straße 2, Darmstadt 64287, Germany. E-mail: [zhuo@ceramics.tu-darmstadt.de](mailto:zhuo@ceramics.tu-darmstadt.de); Prof. Leopoldo Molina-Luna, Advanced Electron Microscopy Division, Department of Materials and Earth Sciences, Technical University of Darmstadt, Peter-Grünberg-Straße 2, Darmstadt 64287, Germany. E-mail: [molina@aem.tu-darmstadt.de](mailto:molina@aem.tu-darmstadt.de)

**How to cite this article:** Jiang T, Pivak Y, Ni F, Gijs van der G, Li J, Zhuo F, Molina-Luna L. Micro-electromechanical system-based cryogenic and heating *in situ* transmission electron microscopy for investigating phase transitions and domain evolution in single-crystal BaTiO<sub>3</sub>. *Microstructures* 2024;4:2024058. <https://dx.doi.org/10.20517/microstructures.2024.50>

**Received:** 18 Jun 2024 **First Decision:** 31 Jul 2024 **Revised:** 6 Sep 2024 **Accepted:** 12 Sep 2024 **Published:** 8 Oct 2024

**Academic Editor:** Dong Su **Copy Editor:** Ting-Ting Hu **Production Editor:** Ting-Ting Hu

## Abstract

Investigating phase transitions between ferroelectric states is crucial for understanding the nucleation, dynamics, and kinetics of domains, both before and after transformation. Here, we assess all phase transitions and domain evolutions in single-crystal BaTiO<sub>3</sub> by implementing microelectromechanical systems (MEMS)-based *in situ* cryogenic (cryo-) and heating transmission electron microscopy (TEM) by continuously varying sample temperatures from -175 °C to 200 °C. Every possible phase-cubic, tetragonal, orthorhombic, and rhombohedral - was identified. An ultra-stable imaging condition was achieved with a mean drift speed of 1.52 nm/min, providing unique opportunities for atomic resolution *in situ* scanning TEM with a wide temperature range. Furthermore, domain nucleation and evolution across phase transitions were investigated using complementary dielectric



© The Author(s) 2024. **Open Access** This article is licensed under a Creative Commons Attribution 4.0 International License (<https://creativecommons.org/licenses/by/4.0/>), which permits unrestricted use, sharing, adaptation, distribution and reproduction in any medium or format, for any purpose, even commercially, as long as you give appropriate credit to the original author(s) and the source, provide a link to the Creative Commons license, and indicate if changes were made.



measurements, optical microscopy, and a phenomenological model. This study underscores the effectiveness and utility of MEMS-based *in situ* cryo-/heating TEM in revealing phase transitions and domain structures in ferroelectric materials.

**Keywords:** *in situ* heating/cryogenic TEM, phase transitions, ferroelectrics, domain nucleation

## INTRODUCTION

Improving tools and methodologies to characterize chemical and physical properties has been essential for studying the relationship between microstructure and macro behaviors, advancing various fields, including material and life sciences. Among all state-of-the-art technologies, *in situ* (scanning) transmission electron microscopy [(S)TEM] offers an irreplaceable advantage by providing direct observations of a sample's response to external stimuli with high spatial resolution, ranging from the micrometer to even picometer scale.

Although the first electron microscope was built in 1932 by Knoll and Ruska<sup>[1]</sup>, it was over 20 years later that the first cryogenic (cryo-) and heating TEM studies were reported, in 1954<sup>[2]</sup> and 1958<sup>[3]</sup>, respectively. Subsequently, there was a burst of developments in *in situ* cryo- and heating TEM particularly in terms of the *in situ* TEM holder and following experimental applications from the 1960s to the 1980s<sup>[4]</sup>. In the early stages, there were two types of heating TEM holders: the ribbon-type and the furnace-type<sup>[4]</sup>. The former had advantages such as instant heating speed, but suffered from disadvantages such as inaccuracy in temperature control and image instability. To improve this, the calibration between the specimen temperature and the input power was essentially required, achieved by observing sharp changes in a material at known temperatures, such as phase transitions in a ferromagnetic material<sup>[5]</sup>. The latter offered uniform heating, excellent temperature stability, and precise temperature control. However, it had the drawback of longer heating times, typically taking 2-5 min to reach equilibrium temperatures<sup>[4]</sup>. Significant improvements to both types of heating holders were achieved through power-input temperature pre-calibration<sup>[6]</sup> and the thermocouple read-out method<sup>[7]</sup>. A substantial decrease in thermal drift was accomplished by thermally insulating the area between the hot stage and the microscope<sup>[8]</sup> and introducing a compensating opposite drift<sup>[9]</sup>. Combining a heating stage with an environmental cell enabled *in situ* observation of the gas-solid interactions inside the microscope from room temperature to over 1500 K<sup>[10-13]</sup>, which was commercially available due to the efforts of Hashimoto *et al.* and Hiziya *et al.*<sup>[14-16]</sup>.

Since the earliest applications of cryo-TEM to the present-day usage, the process has consistently required liquid coolant supplied directly from an external cryostat to the stage<sup>[17]</sup> or a coolant container installed within the microscope<sup>[18]</sup>. According to the different coolants, such as liquid nitrogen<sup>[19]</sup> and helium<sup>[17,18,20-25]</sup>, the operating temperature could be extended from the room temperature to the liquid nitrogen temperature and below 5 K, respectively. In addition to extending the temperature ranges for cryo-TEM, versatility and reliability were also developed in the cooling holder's design and function without sacrificing the spatial resolution<sup>[4,17,26,27]</sup>. These improvements include designing more convenient facilities for specimen exchange, enabling double-tilt capabilities of the stage between millimeter-sized pole pieces, maintaining mechanical stability despite turbulent and boiling coolant circulation, and ensuring thermal stability despite differing thermal expansions in the stage and specimen. Additionally, they involve eliminating contamination from residual vapor condensation inside the microscope during stage cooling, precisely controlling the stage temperature continuously before reaching the lowest temperature limit, and optimizing coolant consumption for greater efficiency. These advancements in cryo-TEM technologies laid the groundwork for later significant breakthroughs in the biological sciences<sup>[28]</sup>, such as in studies of the frozen hydrated

biological specimens<sup>[29-31]</sup>, the vitrification technology<sup>[32,33]</sup> and viruses<sup>[34]</sup>. They also catalyzed progress in material sciences, enabling detailed studies of superconductors<sup>[22]</sup>, solidified gases<sup>[18]</sup>, and magnetic domains<sup>[35]</sup> from the 1960s to the 1980s. Over the subsequent decades, material scientists have pursued more stable working conditions in TEM in order to achieve higher resolution.

Over the last decade, the advancement of aberration-corrected (S)TEM has revolutionized atomic-scale imaging and spectroscopy, making these techniques widely and commonly used. This progress has reignited interest in *in situ* (S)TEM studies, leading to efforts to achieve native observations under various stimuli—such as heating, cooling, environmental (liquid/gaseous), mechanical, and biasing—especially at the atomic scale. Consequently, this high demand is driving the development of ultra-stable, versatile *in situ* TEM holders. For example, Gai *et al.*<sup>[36,37]</sup> focused on developing a heating holder combined with environmental conditions, based on earlier work<sup>[38]</sup>. They pushed the high-temperature limits to over 2000 °C<sup>[39]</sup>, covering the temperature range required for the formation of ceramics, carbon nanotubes, and other materials. They demonstrated *in situ* characterizations of nanoparticle sintering with a resolution close to 1 Å<sup>[39]</sup>. Tai *et al.*<sup>[40]</sup> developed a prototype cryo-holder with an environmental cell in 2014, demonstrating the dynamic process of ice solidification with continuous temperature control between 220 K and 260 K. Later, Bell and Zandbergen<sup>[41]</sup> developed a side-entry JEOL-based cryo-holder in 2016, achieving less than 2 nm/min drift and sub-1 Å resolution in high-resolution TEM (HRTEM) imaging mode. In 2018, a Nion-based, microelectromechanical system (MEMS) chip-compatible, single-tilt version was reported, extending the operating temperature range from liquid nitrogen to ~1000 °C<sup>[42]</sup>. By 2020, Goodge *et al.*<sup>[43]</sup> reported a double-tilt, full-versatility holder with low drift rates of 0.3-0.4 Å/s, capable of sub-1 Å resolution STEM imaging. The rapid advancements in cryo-TEM technology have provided an invaluable tool for mitigating irradiation damage and examining delicate systems at atomic resolution. This has revolutionized the life sciences by revealing the atomic structures of sensitive biomolecules in their native states<sup>[28,44,45]</sup>, a milestone that earned Dubochet the 2017 Nobel Prize in Chemistry<sup>[46]</sup>. Additionally, it has driven advancements in materials sciences<sup>[47]</sup>, including energy storage materials<sup>[48,49]</sup>, soft materials<sup>[50]</sup>, metal-organic frameworks<sup>[51]</sup>, hybrid organic-inorganic halide perovskites<sup>[52]</sup>, and quantum materials<sup>[53-55]</sup>.

Despite many achievements in *in situ* cryo-TEM that have been reported, far less common are *in situ* multi-stimuli or so-called multi-modal TEM studies of the dynamics in ferroelectric materials, especially for covering the low to high temperature range in a single TEM operation. For instance, by applying *in situ* heating TEM, our previous work<sup>[56]</sup> demonstrated the dislocation-mediated domain nucleation and domain wall (DW) pinning in single crystal BaTiO<sub>3</sub> (BTO), where the phase transition of room-temperature tetragonal (T) phase to high-temperature paraelectric phase was observed directly. Ignatans *et al.*<sup>[57,58]</sup> reported local hard and soft pinning effect of 180° DWs in bulk BTO by *in situ* biasing TEM at room temperature and the direct observation of individual Barkhausen pulses by *in situ* biasing TEM at 130 °C. O'Reilly *et al.*<sup>[59]</sup> demonstrated that *in situ* annealing of single-crystal BTO specimens at 800 °C for 5 min in a TEM microscope promotes the reorganization of the domain structure and enhances reproducibility across samples. O'Reilly *et al.*<sup>[60]</sup> presented another case of *in situ* heating in STEM, from room temperature to above the Curie temperature of BTO, but under different environmental conditions, to provide insights into surface-screening mechanisms in domain dynamics. Tsuda *et al.*<sup>[61]</sup> applied cryo-TEM with convergent-beam electron diffraction techniques to demonstrate localized rhombohedral (R) symmetry in the Orthorhombic (O) and T phases of bulk BTO. Mun *et al.*<sup>[62]</sup> also demonstrated a cryo-STEM study on thin film BTO, where atomic-resolution high-angle annular dark-field (HAADF) STEM images were presented at 95 K, 140 K and 300 K, respectively. Both studies lacked continuous control of temperature and were performed using a Gatan cryo-holder. Tyukalova *et al.*<sup>[63]</sup> showed a case of a wide operating temperature range, namely 200 ~ 400 K, using *in situ* heating and cryo-TEM, covering O, T, and cubic (C) phases of

BTO. An ultrahigh dielectric permittivity of [111]-oriented BTO single crystals in the R phase was attributed to the motion of by-produced  $180^\circ$  DWs<sup>[64]</sup>. Nevertheless, there is a critical need for direct observation of phase transitions and domain structures of ferroelectric materials across a broader temperature range. In this work, we applied an *in situ* multi-stimuli TEM to investigate phase transitions and domain evolution in single-crystal BTO, covering a broad temperature range from  $-175^\circ\text{C}$  to  $200^\circ\text{C}$ , using an ultra-stable cryo-TEM holder with intermediate temperature control.

## MATERIALS AND METHODS

In this study, a commercially available [110]-oriented single-crystal BTO (GK EAST Optoelectronic Technologies, Inc., China) was used, which has a dimension of  $4\text{ mm}^3 \times 4\text{ mm}^3 \times 8\text{ mm}^3$ . [001]-oriented samples (defined in the pseudocubic coordinate system) with a dimension of  $4\text{ mm}^3 \times 4\text{ mm}^3 \times 1\text{ mm}^3$  [Supplementary Figure 1] were sliced using a diamond wire saw (model 4240, Well Corporation, Germany) for dielectric measurements. For optical observations, the sliced samples were mechanically polished using an automatic polisher (Phoenix 4000, Jean Wirtz GmbH, Germany). Gold electrodes were sputtered onto two large surfaces using a sputter coater (Emitech K950X, Quorum Technologies Ltd., UK). The TEM specimen was prepared by cutting (001) crystal plane of the BTO sample using a focused ion beam (FIB) in a JIB-4600F MultiBeam System (JEOL, Japan). The as-prepared sample was subsequently mounted on a Thermo Fisher-compatible Heating and Biasing MEMS Nano-chip from DENSSolutions, following the weld-free method reported by Recalde-Benitez *et al.*<sup>[65]</sup>. To eliminate residual stress during sample preparation, all investigated samples were further annealed at  $200^\circ\text{C}$  for 2 h.

Dielectric permittivity measurements were obtained using an HP 4192A impedance analyzer (Hewlett Packard, USA) in the range from room temperature to  $200^\circ\text{C}$ . These measurements were conducted under a 1 V root-mean-square (RMS) biasing field, utilizing a furnace (Nabertherm Inc., Germany) with a temperature ramp set at  $1^\circ\text{C}/\text{min}$ . For measurements below room temperature, an impedance analyzer (Alpha-A, Novocontrol Technologies, Germany) equipped with a cryostat was used, also with a temperature ramp of  $1^\circ\text{C}/\text{min}$ . Optical images were collected using an Axio Imager2 microscope (Zeiss, Oberkochen, Germany) equipped with a heating/cooling stage (HFS600E-PB4, Linkam Scientific Instruments, UK). Imaging was performed under differential interference contrast (DIC) and reflection modes. Bright-field (BF)-TEM experiments were conducted utilizing a Thermo Fisher Scientific Spectra 300 (Thermo Fisher Scientific, Inc., USA), operating at an acceleration voltage of 300 kV. The spot size 2 and the C2 condenser aperture of  $150\ \mu\text{m}$  were adopted. The objective aperture was  $10\ \mu\text{m}$ . The beam current was 3 nA. To acquire HAADF STEM images, the camera length was adopted as 115 mm. C2 aperture was  $50\ \mu\text{m}$ . The convergence semiangle was  $21.5\ \text{mrad}$ . The collection angle of HAADF STEM imaging was  $50\text{--}200\ \text{mrad}$ . The beam current was 50 pA. The multi-stimuli *in situ* TEM experiments, incorporating both cryo- and heating processes, were conducted using a double-tilt DENSSolutions Lightning Arctic holder<sup>[66]</sup> [Figure 1A]. BF-TEM images were acquired sequentially with a constant frame rate of 750 ms/frame. The temperature of the TEM specimen was increased from  $-175^\circ\text{C}$  to  $200^\circ\text{C}$  at a rate of  $10^\circ\text{C}/\text{min}$ , with pauses at  $-90^\circ\text{C}$ ,  $10^\circ\text{C}$ ,  $135^\circ\text{C}$ , and  $175^\circ\text{C}$ , each lasting 3 min. After maintaining the specimen at  $200^\circ\text{C}$  for more than 13 min, it was cooled down to  $-175^\circ\text{C}$  with the same rate, with pauses at  $135^\circ\text{C}$ ,  $50^\circ\text{C}$ ,  $10^\circ\text{C}$ , and  $-90^\circ\text{C}$ , each lasting 3 min.

## RESULTS AND DISCUSSION

A DENSSolutions Heating and Biasing chip (Thermo Fisher-compatible) was employed for the *in situ* TEM experiments, as featured in Figure 1B. This MEMS-based chip contains six electrical contacts, of which four are dedicated to control resistive heating and the remaining two are used to apply biasing stimuli [Figure 1B]. The tip of the holder is connected to a metal cooling braid via a cooling rod running through

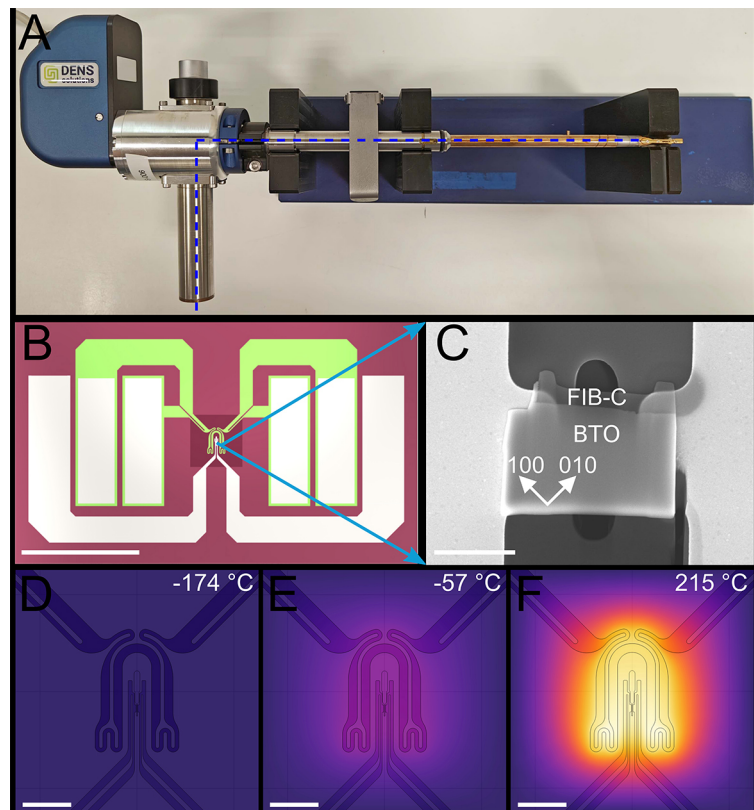


**Figure 1.** A: A DENSsolutions Lightning Arctic TEM holder for *in situ* biasing, heating, and cryo- experiments. The tip of the holder is internally connected to the metallic cooling braid that is immersed in liquid nitrogen, as depicted by the blue dashed line; B: thermo Fisher-compatible heating and biasing nano-chip for *in situ* TEM experiments. The scale bar is 2 mm; C: a representative SEM image of the FIB-prepared single-crystal BTO specimen on the nano-chip. A carbon protection layer (marked as FIB-C) was deposited on the top of BTO sample. The scale bar is 2  $\mu\text{m}$ ; D-F: finite element analysis simulations of the temperature distribution in the sample area during heating at a few set temperatures, namely -174  $^{\circ}\text{C}$ , -57  $^{\circ}\text{C}$  and 215  $^{\circ}\text{C}$  while the holder is being cooled. The scale bars are 100  $\mu\text{m}$ . TEM: transmission electron microscopy; BTO:  $\text{BaTiO}_3$ ; FIB: focused ion beam; SEM: scanning electron microscope.

the holder. The cooling braid, attached to the back side of the holder, is immersed in a non-integrated liquid nitrogen dewar. Once the holder is cooled and stabilized, the heater on the nanochip can be activated to heat the TEM specimen locally to the desired temperature above the cryo-baseline, covering a temperature range from  $-175 \pm 9$   $^{\circ}\text{C}$  to the maximum temperature of  $800 \pm 40$   $^{\circ}\text{C}$  or  $1300 \pm 65$   $^{\circ}\text{C}$ , depending on the exact chip used, e.g., heating and biasing or heating only, respectively. The temperature calibration of the MEMS-based chip uses a linear relationship between the resistance of the heater and the temperature or by analyzing the infrared radiation produced by MEMS-based *in situ* systems<sup>[67-70]</sup>. More detailed characterization of the temperature calibration of the nano-chips in low and high temperature ranges will be reported elsewhere.

As shown in [Figure 1C](#), a carbon protection layer (marked as FIB-C) was deposited on top of the BTO sample. This carbon protection layer does not significantly alter the domain dynamics due to its amorphous nature and minimal mechanical impact. The FIB-prepared TEM specimen, with dimensions of approximately  $4 \mu\text{m}^2 \times 3 \mu\text{m}^2$  and a thickness of about 150 nm, was mounted on the window between two platinum pads solely through van der Waals forces<sup>[65]</sup>, resulting in a free mechanical boundary condition for the ferroelectric TEM specimen. The BTO specimen was heated using a defined step-by-step temperature profile ramp. To validate the temperature distribution generated by the MEMS heater while the tip is being cooled, we carried out a finite element analysis using COMSOL Multiphysics<sup>[71]</sup>. As depicted in [Figure 1D-F](#),

the temperature distribution is homogeneous in the sample region at various temperatures. By using this experimental setup, we were able to observe phase transitions and domain features within a temperature range from -175 °C to 200 °C, covering the well-known phase transitions of BTO.

To validate the ultra-high stability of this *in situ* TEM holder at cryo-temperatures, capable of acquiring the atomic resolution HAADF STEM image, a sequential of ten frames of HAADF STEM images were obtained on this single-crystal BTO TEM specimen along the [001] zone axis. Each frame of the HAADF STEM image (2048 pixels × 2048 pixels) was captured within 1.29 s, resulting in 12.87 s in total for ten frames. The first frame is present in [Figure 2A](#). The field of view of the HAADF STEM images is 18.37 nm × 18.37 nm. No obvious lattice distortion is observed due to the sample drift. To quantify the drift speed of the TEM specimen at cryo-temperature, the drift trajectory of a single Ba atomic column, representing the drift of the whole TEM specimen, is recorded by tracking the position of this single atomic column in sequential frames, as shown in [Figure 2B](#). The starting point of this Ba atomic column is assigned as the origin. The direction and spread of position changes are shown by an arrow with gradient transparency. The average drift speed throughout the acquisition period is calculated to be 1.52 nm/min.

To estimate the phase transition temperatures of BTO, we measured the bulk BTO sample with the same orientation during the heating process. Below -87 °C, our sample exhibited a Rhombohedral (R3m crystal structure) phase with a relative dielectric permittivity of 1600 [[Figure 3A](#)] and permissible eight spontaneous polarization vectors [[Supplementary Figure 2](#)]. The phase transition from the R phase to the O occurs at -87 °C, accompanied by a dielectric anomaly [[Figure 3A](#)]. The O phase has twelve spontaneous polarization vectors pointing toward the center of each edge of the unit cell [[Supplementary Figure 2](#)]. With increasing temperature, the O phase transforms into a T (P4mm crystal structure) phase with four spontaneous polarizations [[Supplementary Figure 2](#)] at around 12 °C, accompanied by a significant jump in the relative permittivity ( $\Delta\epsilon_{33}/\epsilon_0 = 2000$ ). Above this transition temperature, the permittivity decreased first and then increased up to the Curie temperature ( $T_C = 132$  °C). With further increasing the temperature, the permittivity decreased. Note that the permittivity values in the R, O and T phases measured in this work were higher than those reported in the mono-domain BTO crystal with the same orientation<sup>[72,73]</sup> suggesting that our BTO sample has multi-domain states in the ferroelectric phases<sup>[74,75]</sup>. The experimentally observed dielectric permittivity cannot be accurately calculated without further knowledge of the complex domain structure within the crystal.

According to the Landau-Devonshire phenomenological model, the phase transition properties of single-domain BTO crystals can be described using a limited number of parameters. The bulk Landau free-energy density is expressed as an eighth-order polynomial expansion<sup>[76-78]</sup>:

$$\begin{aligned} f_{\text{bulk}} = & \alpha_1 (P_1^2 + P_2^2 + P_3^2) + \alpha_{11} (P_1^4 + P_2^4 + P_3^4) + \alpha_{12} (P_1^2 P_2^2 + P_1^2 P_3^2 + P_2^2 P_3^2) + \\ & \alpha_{111} (P_1^6 + P_2^6 + P_3^6) + \alpha_{112} (P_1^2 (P_2^4 + P_3^4) + P_2^2 (P_1^4 + P_3^4) + P_3^2 (P_1^4 + P_2^4)) + \\ & \alpha_{123} P_1^2 P_2^2 P_3^2 + \alpha_{1111} (P_1^8 + P_2^8 + P_3^8) + \alpha_{1112} (P_1^6 (P_2^2 + P_3^2) + P_2^6 (P_1^2 + P_3^2) + \\ & P_3^6 (P_1^2 + P_2^2)) + \alpha_{1122} (P_1^4 P_2^4 + P_2^4 P_3^4 + P_1^4 P_3^4) + \alpha_{1123} (P_1^4 P_2^2 P_3^2 + P_2^4 P_1^2 P_3^2 + \\ & P_3^4 P_1^2 P_2^2) \end{aligned} \quad (1)$$

Where  $\alpha_{ij}$ ,  $\alpha_{ijkl}$ ,  $\alpha_{ijklmn}$  and  $\alpha_{ijklmnop}$  are the Landau coefficients. We assume that only  $\alpha_{ij}$  are linearly dependent on temperature and the others are constants. The material parameters can be found in [Supplementary Table 1](#). [Figure 3B](#) presents the calculated spherical maps of bulk-free energy for the different phases. In the C phase, the energy distribution is homogeneous, reflecting its symmetric and stable nature. Upon cooling from above the Curie temperature, the T phase emerges, characterized by four distinct regions (i.e., the four possible orientations of polarization vectors within the T crystal structure) of energy minima corresponding to the spontaneous polarization directions [[Supplementary Figure 2](#)]. Further cooling leads to the O phase, displaying twelve local minima that align with the polarization vectors toward the edges of the unit cell [[Supplementary Figure 2](#)]. Finally, the R phase exhibits eight regions of low

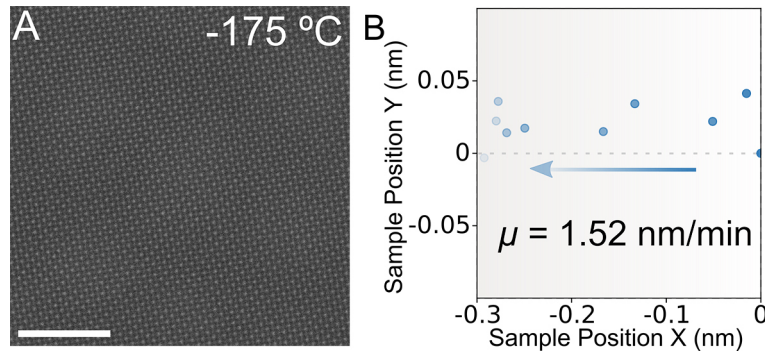


**Figure 2.** Drift analysis in the cryo-STEM experiment at -175 °C. A: A representative HAADF STEM image from a sequence of 10 frames. The scale bar is 5 nm; B: the drift trajectory of a sample, indicated by the arrow showing the direction and spread of position changes over time. The origin presents the starting position. STEM: scanning transmission electron microscopy; HAADF: high-angle annular dark-field.

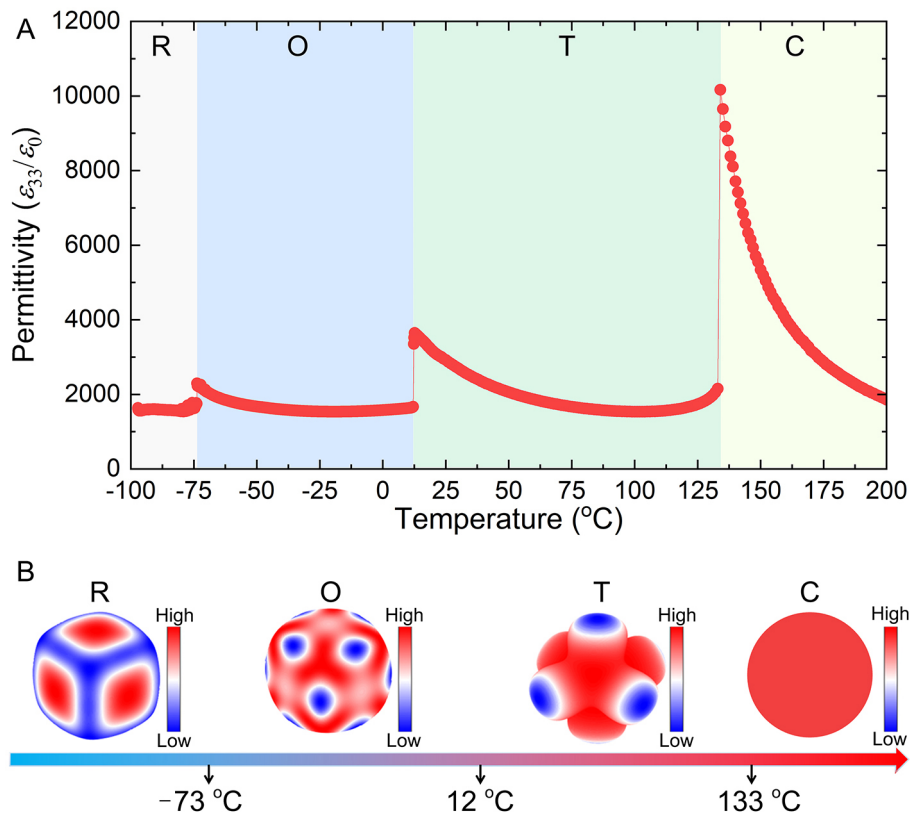


**Figure 3.** A: Temperature dependence of relative dielectric permittivity ( $\epsilon_{33}/\epsilon_0$ ) of the investigated single-crystal BTO sample measured at 1 kHz; B: calculated spherical map of bulk-free energy for C, T, O and R phases. The favored polarization vectors point toward regions with local energy minima (blue). The C phase represents a uniformly nonpolar state without distinct domains. R: Rhombohedral phases; O: orthorhombic; T: tetragonal; C: cubic; BTO: BaTiO<sub>3</sub>.

energy<sup>[79]</sup>, correlating with the spontaneous polarization directions [Supplementary Figure 2]. This comprehensive data illustrates the intricate relationship between temperature, dielectric permittivity, and phase transitions in BTO single crystals. The transitions from R to O, T, and finally to C phase highlight the complex structural changes that significantly influence the dielectric properties of the material. Understanding these transitions is crucial for manipulating and utilizing BTO in practical applications such

as capacitors, sensors, and actuators, where precise control of dielectric properties is essential. The Landau-Devonshire model, coupled with the empirical data presented, offers a robust framework for predicting and explaining these phase transitions and their impact on material performance. The energy equivalence of various spontaneous polarization directions results in the formation of ferroelectric domain structures, which significantly influence the electrical properties of the material.

To monitor domain nucleation and evolution during the above-mentioned phase transitions, the *in situ* cryo- and heating TEM characterization is conducted on a single-crystal BTO specimen. The orientation of BTO specimen is further confirmed by the selected area electron diffraction (SAED) pattern taken at  $-160$  °C, see [Supplementary Figure 3](#). At  $-150$  °C, both  $71^\circ$  and  $180^\circ$  DWs in the R phase are observed, which are not edge-on walls as shown in the BF-TEM image [[Figure 4A](#) and see schematics of these domain configurations in [Supplementary Figure 4A](#)]. Note that the  $71^\circ$  and  $180^\circ$  DWs have  $0^\circ$  and  $\sim 27^\circ$  with respect to the reference  $[010]$  direction, respectively. Interestingly, a zigzag pattern composed of both  $60^\circ$  and  $120^\circ$  DWs is featured in the O phase [see the BF-TEM image obtained at  $-60$  °C in [Figure 4B](#) and schematics in [Supplementary Figure 4B](#)]. The normal of these  $60^\circ$  DWs rotates with increasing temperature, rather than remaining fixed to any crystallographic axis<sup>[80]</sup>, as seen in [Supplementary Video 1](#). This zigzag to stripe pattern transition between O and T phases in BTO crystal was previously observed by piezoresponse force microscopy<sup>[75]</sup>. Additionally, edge-on  $90^\circ$  DWs are captured in the O phase, with the walls running along the  $[010]$  crystallographic axis. Note that both  $120^\circ$  and  $90^\circ$  DWs have walls parallel to the  $[010]$  direction, while the  $120^\circ$  DWs are not imaged edge-on. With further heating above the transition temperature of O phase to T phase, we document *a-a* and *a-c* type  $90^\circ$  ferroelastic DWs [see the BF-TEM image obtained at  $50$  °C in [Figure 4C](#) and [Supplementary Figure 4C](#)], with the boundaries running along the  $[010]$  and  $[110]$  crystallographic axes, respectively. The *a-c* type  $90^\circ$  DWs vanish and transform into *a-a* type  $90^\circ$  DWs once the temperature is higher than  $60$  °C [[Figure 4D](#)]. As the temperature approaches the  $T_C$ , the *a-c* needle DWs disappear. Above  $T_C$ , no distinct domain features are observed [see the BF-TEM image obtained at  $200$  °C in [Figure 4E](#)]. The stripe-like color contrasts in the image were typical bending contours in this case<sup>[81,82]</sup>. Detailed temperature profile is shown in [Figure 4F](#) and domain evolution during the complete *in situ* heating TEM process is provided in [Supplementary Video 1](#).

[Figure 5](#) offers a comprehensive view of the domain evolutions observed through *in situ* cooling/cryo-TEM characterization across a range of temperatures, from the high-temperature C phase to the R phase at cryo-temperatures. Below the  $T_C$ , the nucleation of needle-like domains and *a<sub>1</sub>-a<sub>2</sub>*  $90^\circ$  DWs are present, remaining stable below  $T_C$ . This phenomenon is attributed to the large permittivity response of BTO, which arises from dielectric tensor anisotropy<sup>[82,83]</sup>, where the permittivity of *a* domains significantly exceeds that of *c* domains ( $\epsilon_a > \epsilon_c$ ). Specifically, at  $75$  °C, the BF-TEM image [[Figure 5B](#)] reveals the edge-on *a<sub>1</sub>-a<sub>2</sub>*  $90^\circ$  domains. As the temperature decreases, these  $90^\circ$  *a-a* type DWs transform into *a-c*  $90^\circ$  lamellar DWs below a certain temperature, with the domain boundaries becoming almost parallel to the  $[010]$  direction. This increase in DW density and the reduction in domain size may contribute to the observed rise in permittivity prior to the T-to-O phase transition, as seen in [Figure 3](#). To double check the evolutions of domain structures in single-crystal BTO, we capture optical images as the temperature decreases from  $140$  °C to  $30$  °C. At  $140$  °C, the material is in the C phase, with no distinct domain structures visible [[Supplementary Figure 5](#)]. As the temperature drops to between  $131$  °C and  $126$  °C, *a<sub>1</sub>/a<sub>2</sub>* DWs projected along the  $\langle 110 \rangle_{pc}$  axis begin to appear, indicating the transition to the T phase. In the temperature range of  $128$  °C to  $122$  °C, both *a<sub>1</sub>/a<sub>2</sub>* and *a/c* domains coexist. Further cooling to temperatures between  $120$  °C and  $30$  °C shows an increase in the density and complexity of the DWs, with well-defined *a<sub>1</sub>/a<sub>2</sub>* and *a/c* domains. The detailed domain nucleation and evolution processes during cooling from  $140$  °C to  $30$  °C are provided in [Supplementary Video 2](#). Our optical microscopy results are in good agreement with the TEM observations



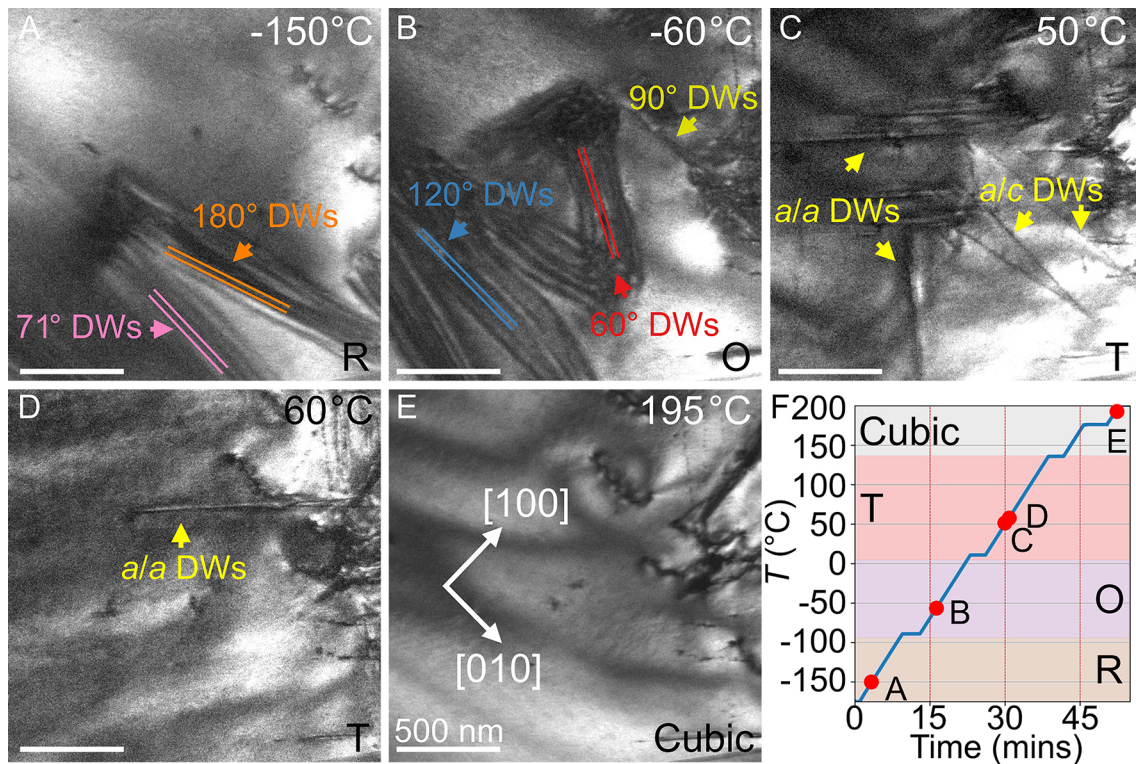


**Figure 4.** A-E: Representative BF TEM images obtained along [001] zone axis of the BTO sample during *in situ* heating process. The scale bars are 500 nm; F: the plot shows temperature ( $T$ ) vs. time, with points A-E highlighted at different temperatures, corresponding to BF-TEM images labeled A-E. T: Tetragonal; R: rhombohedral phases; O: orthorhombic; TEM: transmission electron microscopy; BTO: BaTiO<sub>3</sub>; BF: bright-field; DW: domain wall.

during the cooling process across the C-to-T phase transition. The transformation in the domain configuration from *a-a* to *a-c* mirrors the behavior previously observed in low-strain BTO thin films<sup>[84]</sup> and is similar to recent findings in TEM specimens of BTO<sup>[58,60,63]</sup> This reconfiguration might be attributed to the material undergoing the subsequent low-temperature phase transition from T to O<sup>[85]</sup>, possibly facilitated by the low-strain conditions of the BTO sample. In the O phase, at -50 °C, non-edge-on 120° DWs oriented along the [010] reference direction are captured [Figure 5D]. These DWs are indicative of the structural adjustments BTO undergoes as it transitions from the T phase. Furthermore, in the R phase, observed at -175 °C, we document non-ferroelastic 180° DWs, along with ferroelastic 71° and 109° DWs [Figure 5E]. For a wall that is not imaged edge-on, it corresponds to the 71° DW. For the edge-on DW marked by the red arrow in Figure 5E, it could be attributed to either a neutral 109° DW or a charged 71° DW. These variations in DW types and orientations highlight the complex interplay of structural and ferroelectric properties in BTO as it cools through different phase transitions. The cooling process, depicted stepwise in Figure 5F, elucidates the sequential nature of these phase transitions and domain evolutions. The detailed domain evolution during the cooling process is provided in Supplementary Video 3.

In ferroelectric materials, spontaneous electric polarization is typically coupled with spontaneous mechanical strain, forming domains with uniform dipole and strain. While domain formation reduces elastic strain and depolarization fields, it introduces gradients of spontaneous strain and electrical charge between adjacent domains, thereby increasing the energy due to DWs. The equilibrium domain structure in ferroelectrics is such that it minimizes the total energy resulting from these effects<sup>[86,87]</sup>. To reduce the spontaneous strain gradient, DWs ideally form on planes where the spontaneous strain is identical for both

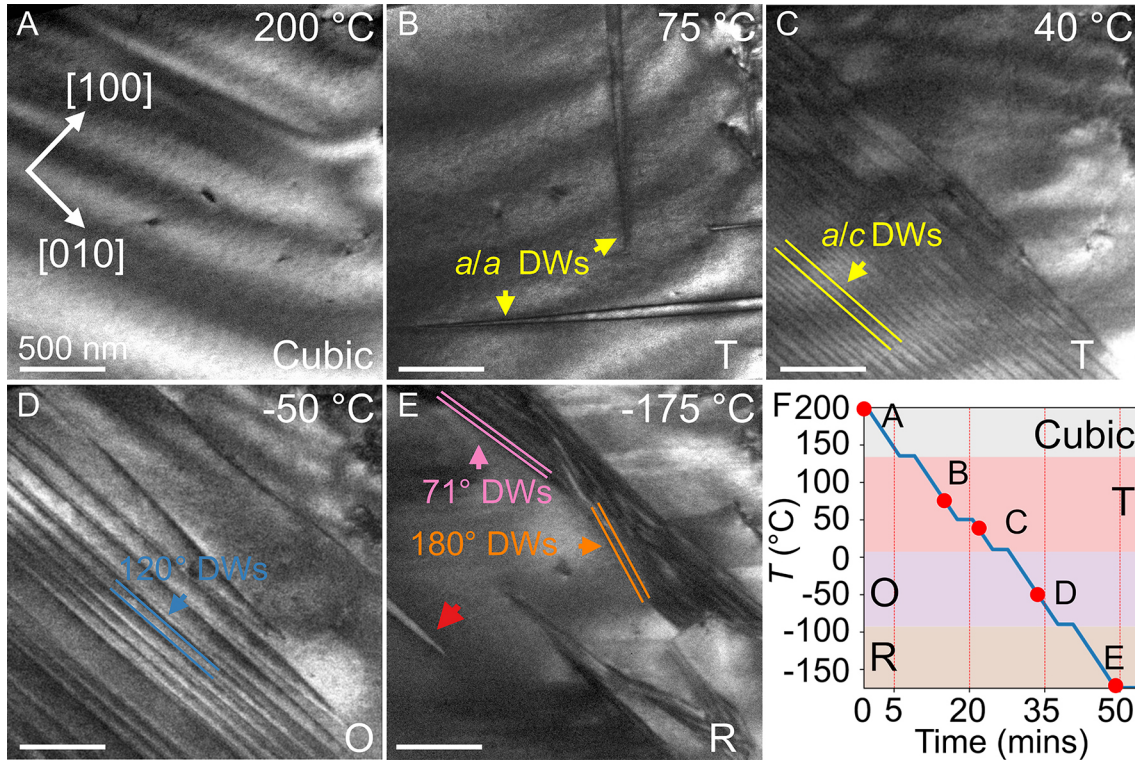


**Figure 5.** *In situ* cooling TEM characterization of all four phases of BTO. A-E: BF TEM images obtained along [001] zone axis of the BTO sample. The scale bars are 500 nm; F: the plot shows temperature ( $T$ ) vs. time, with points A-E highlighted at different temperatures, corresponding to BF-TEM images labeled A-E. T: Tetragonal; R: rhombohedral phases; O: orthorhombic; TEM: transmission electron microscopy; BTO: BaTiO<sub>3</sub>; BF: bright-field; DW: domain wall.

domains in any direction within the plane. These are termed permissible walls. Additionally, ferroelectric DWs are usually charge-free, meaning the spontaneous polarization on either side results in no net electrical charge, thus forming neutral DWs. When two domains with different spontaneous polarizations meet, the polarization vector and strain tensor transition from one state  $[P(-\infty), e(-\infty)]$  to another state  $[P(+\infty), e(+\infty)]$ . In the transition region, DWs with specific orientations are formed. The normal vector of the DW,  $\mathbf{n} = (x_1, x_2, x_3)$ , of the DWs must satisfy mechanical compatibility conditions<sup>[80,88,89]</sup>:

$$\sum_{i,j=1}^3 [e_{ij}(+\infty) - e_{ij}(-\infty)] x_i x_j = 0 \quad (2)$$

where  $e_{ij}(+\infty)$  and  $e_{ij}(-\infty)$  are the components of the spontaneous strain tensor in each domain, and  $X_m, X_n$  are the geometric coordinates. DWs can be classified into ferroelastic and non-ferroelastic types based on their ferroelastic properties. Non-ferroelastic DWs, where the spontaneous polarization vectors on either side are antiparallel, are referred to as 180° DWs. These DWs satisfy the condition  $e_{ij}(+\infty) - e_{ij}(-\infty) = 0$ , thus  $N = \infty$ . Ferroelastic DWs, where the spontaneous polarization vectors are not parallel, are known as non-180° DWs, with  $N = 2$ . As a result, 12 typical types of neutral DWs that meet mechanical compatibility in BTO system, identified by the phase structure (R, O, T) and the angle between the spontaneous polarization vectors (180°, 120°, 109°, 90°, 71°, 60°).

Based on our MEMS-based *in situ* cryo-/heating TEM results, we summarized the observed orientations of these DWs in Table 1. Note that the O60 DW is a typical S-type DW, whose normal direction  $\mathbf{n}_{O60}$  is determined by the material's spontaneous strain tensor<sup>[80]</sup>. The detailed set of plausible neutral and

**Table 1. Cartesian components of boundary conditions and domain-wall normal vectors for polarizations in adjacent domain states for the inspected DWs**

Wall	$\mathbf{P}(-\infty)$	$\mathbf{P}(+\infty)$	DW normal vector
T90	(1, 0, 0)	(0, -1, 0)	$(\frac{1}{\sqrt{2}}, \frac{-1}{\sqrt{2}}, 0)$
T180	(1, 0, 0)	(-1, 0, 0)	$(0, \frac{1}{\sqrt{2}}, \frac{1}{\sqrt{2}})$
O90	$(\frac{1}{\sqrt{2}}, \frac{i}{\sqrt{2}}, 0)$	$(\frac{1}{\sqrt{2}}, \frac{-1}{\sqrt{2}}, 0)$	(1, 0, 0)
O180	$(\frac{1}{\sqrt{2}}, \frac{1}{\sqrt{2}}, 0)$	$(\frac{-1}{\sqrt{2}}, \frac{-1}{\sqrt{2}}, 0)$	$(\frac{1}{\sqrt{2}}, \frac{-1}{\sqrt{2}}, 0)$
O60	$(\frac{1}{\sqrt{2}}, \frac{1}{\sqrt{2}}, 0)$	$(0, \frac{1}{\sqrt{2}}, \frac{-1}{\sqrt{2}})$	$\mathbf{n}_{\text{O60}}$
O120	$(\frac{1}{\sqrt{2}}, \frac{1}{\sqrt{2}}, 0)$	$(0, \frac{-1}{\sqrt{2}}, \frac{1}{\sqrt{2}})$	$(\frac{1}{\sqrt{2}}, 0, \frac{1}{\sqrt{2}})$
R180{2 11}	$(\frac{1}{\sqrt{3}}, \frac{1}{\sqrt{3}}, \frac{1}{\sqrt{3}})$	$(\frac{-1}{\sqrt{3}}, \frac{-1}{\sqrt{3}}, \frac{1}{\sqrt{3}})$	$(\frac{-2}{\sqrt{6}}, \frac{1}{\sqrt{6}}, \frac{1}{\sqrt{6}})$
R109	$(\frac{1}{\sqrt{3}}, \frac{1}{\sqrt{3}}, \frac{1}{\sqrt{3}})$	$(\frac{-1}{\sqrt{3}}, \frac{-1}{\sqrt{3}}, \frac{1}{\sqrt{3}})$	(0, 0, 1)
R71	$(\frac{1}{\sqrt{3}}, \frac{1}{\sqrt{3}}, \frac{1}{\sqrt{3}})$	$(\frac{-1}{\sqrt{3}}, \frac{-1}{\sqrt{3}}, \frac{1}{\sqrt{3}})$	$(\frac{1}{\sqrt{2}}, 0, \frac{1}{\sqrt{2}})$

DW: Domain wall.

mechanically compatible DW types is schematically displayed in [Supplementary Figure 4](#). It is noted that we are not able to find all permissible DWs in BTO; for instance, 180° DWs are not visible in the T phase in our BTO lamellae. It should be noted that 180° DWs in the T or O phase do not have a well-defined direction as they usually exhibit a meandering morphology in experiments. This may be caused by the DWs projected along the  $\langle 100 \rangle$  pc or  $\langle 010 \rangle$  pc axis, but not visible on the (001) planes. Our observations provide a detailed understanding of the domain dynamics in BTO single crystals, emphasizing how temperature variations influence the formation and stability of different domain structures. The *in situ* TEM characterization allows for real-time monitoring of these changes, offering valuable insights into the fundamental mechanisms governing the ferroelectric and ferroelastic properties of BTO. This knowledge is crucial for optimizing the material's performance in various applications<sup>[84,90]</sup>, including capacitors, sensors, and actuators, where precise control over domain configurations and transitions can significantly enhance functionality.

## CONCLUSIONS

In this study, we demonstrated HAADF STEM imaging under ultra-stable conditions with an average drift speed of 1.52 nm/min at the cryo-temperature, providing unparalleled opportunities for atomic-resolution *in situ* STEM imaging over a wide temperature range. We employed *in situ* cooling and heating TEM to investigate the phase transitions and the evolutions of ferroelectric-ferroelastic domains in single-crystal BTO vs. temperature varied in a continuous manner. By cycling the sample through a wide temperature range from -175 °C to 200 °C in a single *in situ* TEM experiment, encompassing the Curie temperature and the transition temperatures between the T, O, and R phases, we were able to examine the intricate behavior of the domains and DWs. We confirmed that BTO exhibits distinct domain structures and DW configurations in different phases. Specifically, we observed a dense, metastable configuration of competing *a-c* and *a-a* domain variants visualized through TEM. These observations were further corroborated by *in situ* cooling optical microscopy studies. The formation and behavior of different DWs were identified for all mechanically compatible and electrically neutral domain-wall types throughout the entire temperature range of the ferroelectric phases. To the best of our knowledge, this is the first time such experimental techniques have been utilized in this context. This novel approach allowed us to capture real-time changes in domain structures as the material underwent various phase transitions. The detailed mapping of domain-wall dynamics and phase transitions may offer invaluable insights that can improve theoretical models and simulations, thereby contributing to a deeper understanding of the fundamental mechanisms governing ferroelectric behavior.

The demonstration of the capabilities of the presented MEMS-based *in situ* TEM holder represents a promising step toward studying ferroic phase transitions across a continuous cryo-temperature range. In the near-future findings that combining a wide temperature range together with electrical stimuli will be presented. Furthermore, this study paves the way for future experimental and theoretical investigations using *in situ* heating and cooling TEM techniques. The successful application of these techniques to BTO suggests that they could be similarly applied to other ferroelectric materials, potentially leading to new discoveries and advancements in the field. Future research could explore the effects of external electric fields, mechanical stresses, charge distribution, and defect structures such as oxygen vacancies<sup>[91]</sup> and dislocations<sup>[56,92,93]</sup> on domain behavior and phase transitions. Our study demonstrates the power and utility of MEMS-based *in situ* TEM methods for studying the dynamic behavior of ferroelectric materials. The comprehensive analysis of BTO provided by this work not only advances our understanding of its phase transitions and domain dynamics, but also sets the stage for further research and development in the field of functional materials such as ferroelectrics and superconductors.

## DECLARATIONS

### Acknowledgements

We thank Dr. Chen Li and Dr. Mauro Porcu for their kind assistance and access to the latest instrumentation at the Thermo Fisher Scientific Center for Electron Microscopy (*NanoPort*) in the Netherlands. Tianshu Jiang, Yevheniy Pivak, and Leopoldo Molina-Luna undertook the electron microscopy analysis, and *in situ* TEM method development. Gijs van der Gugten conducted the Finite Element Analysis simulations, and Junjie Li conducted the theoretical calculations of Landau free-energy density. Fangping Zhuo provided the BaTiO<sub>3</sub> sample, obtained optical images, and contributed to the interpretation of the results. We thank Dr. Alexander Zintler for helpful discussions.

### Authors' contributions

The conception and design of the work: Jiang T, Zhuo F, Molina-Luna L

Provided material: Zhuo F

The acquisition and analysis of data: Jiang T, Zhuo F, Pivak Y, Li J, Ni F, Molina-Luna L

The interpretation of data: Jiang T, Zhuo F, Molina-Luna L

The writing and revising: Jiang T, Zhuo F, Molina-Luna L

Writing and reviewing the manuscript: Jiang T, Pivak Y, Ni F, van der Gugten G, Li J, Zhuo F, Molina-Luna L

### Availability of data and materials

The data that support the findings of this study are available from the corresponding author upon reasonable request.

### Financial support and sponsorship

This work was supported by the German Research Foundation (DFG) through project nos (414179371) and (530438323). Jiang T and Molina-Luna L acknowledge the European Research Council (ERC) under Grant Nos. (805359-FOXON), (957521-STARE) and (101088712-ELECTRON). Zhuo F acknowledges the seed fund provided by Matter and Materials at TU Darmstadt project no. (40101529).

### Conflicts of interest

Yevheniy Pivak and Gijs van der Gugten are affiliated with DENSSolutions BV, while the other authors have declared that they have no conflicts of interest.

## Ethical approval and consent to participate

Not applicable.

## Consent for publication

Not applicable.

## Copyright

© The Author(s) 2024.

## REFERENCES

1. Knoll M, Ruska E. Das Elektronenmikroskop. *Z Physik* 1932;78:318-39. DOI
2. Leisegang S, Ross R R. Versuch mit einer kuehlbaren objektpatrone. In: Ross R, editors. Proceedings of the third international congress on electron microscopy. Royal Society London; 1954. pp. 184-88. Available from: [https://scholar.google.com/scholar?hl=zh-CN&as\\_sdt=0%2C5&q=Leisegang+S.+Versuch+mit+einer+Kuehlbaren+Objektpatrone.+In%3A+Ross+R%2C+editors.+The+third+International+Congress+on+Electron+Microscopy%3A+Proceedings+of+the+Third+International+Congress+on+Electron+Microscopy%3B+1954&btnG=](https://scholar.google.com/scholar?hl=zh-CN&as_sdt=0%2C5&q=Leisegang+S.+Versuch+mit+einer+Kuehlbaren+Objektpatrone.+In%3A+Ross+R%2C+editors.+The+third+International+Congress+on+Electron+Microscopy%3A+Proceedings+of+the+Third+International+Congress+on+Electron+Microscopy%3B+1954&btnG=) [Last accessed on 8 Oct 2024].
3. Whelan MJ. A high temperature stage for the Elmiskop I. In: Bargmann W, Möllenstedt G, Niehrs H, Peters D, Ruska E, Wolpers C, editors. Verhandlungen. Berlin: Springer Berlin Heidelberg; 1960. p. 96-100. DOI
4. Butler EP. In situ experiments in the transmission electron microscope. *Rep Prog Phys* 1979;42:833-95. DOI
5. Martin CJ, Boyd JD. A method for calibrating a specimen-heating stage in the electron microscope. *J Phys E: Sci Instrum* 1973;6:21-2. DOI
6. Clark JB. High-temperature, high-resolution metallography. *Metallurgical society conference* 1965;38:347. Available from: <https://cir.nii.ac.jp/crid/1570291224290647040> [Last accessed on 8 Oct 2024].
7. Jouffrey B, Favard P. Microscopie électronique à haute tension 1975: textes des communications présentées au 4e congrès international, toulouse, 1-4 septembre 1975. Societe Francaise de Microscopie Electronique; 1976. p. 345. Available from: [https://scholar.google.com/scholar?hl=zh-CN&as\\_sdt=0%2C5&q=Jouffrey+B%2C+Favard+P.+Microscopie+%C3%89lectronique+%C3%80+Haute+Tension+1975%3A+Textes+Des+Communications+Pr%C3%A9sent%C3%A9es+Au+4e+Congr%C3%A8s+International%2C+Toulouse%2C+1-4+September+1975.+Societe+Francaise+de+Microscopie+Electronique%3B+1976.+pp.+345&btnG=](https://scholar.google.com/scholar?hl=zh-CN&as_sdt=0%2C5&q=Jouffrey+B%2C+Favard+P.+Microscopie+%C3%89lectronique+%C3%80+Haute+Tension+1975%3A+Textes+Des+Communications+Pr%C3%A9sent%C3%A9es+Au+4e+Congr%C3%A8s+International%2C+Toulouse%2C+1-4+September+1975.+Societe+Francaise+de+Microscopie+Electronique%3B+1976.+pp.+345&btnG=) [Last accessed on 8 Oct 2024].
8. Swann PR, Humphreys CJ, Goringe MJ. High voltage electron microscopy. In: Peter Roland Swann, editors. Blackwell Scientific Publications; 1973. p.365. Available from: <https://web.cecs.pdx.edu/~cgshir/Glenns%20Publications/02%201974%20Critical%20Voltage%20Effect%20and%20Applications%20Thomas%20Shirley%20Lally%20Fisher.pdf> [Last accessed on 8 Oct 2024].
9. Tejada A, den Dekker AJ. A comparison between minimum variance control and other online compensation methods for specimen drift in transmission electron microscopy. *Multidim Syst Sign Process* 2014;25:247-71. DOI
10. Baker R, Feates F, Harris P. Continuous electron microscopic observation of carbonaceous deposits formed on graphite and silica surfaces. *Carbon* 1972;10:93-6. DOI
11. Baker R. Nucleation and growth of carbon deposits from the nickel catalyzed decomposition of acetylene. *Journal of Catalysis* 1972;26:51-62. DOI
12. Baker RTK, Harris PS. Controlled atmosphere electron microscopy. *J Phys E: Sci Instrum* 1972;5:793-7. DOI
13. Fujita H, Komatsu M, Ishikawa I. A universal environmental cell for a 3MV-class electron microscope and its applications to metallurgical subjects. *Jpn J Appl Phys* 1976;15:2221-8. DOI
14. Hashimoto H, Naiki T, Eto T, Fujiwara K. High temperature gas reaction specimen chamber for an electron microscope. *Jpn J Appl Phys* 1968;7:946. DOI
15. Hiziya K, Hashimoto H, Watanabe M, Mihama K. Gas reaction on the specimen. In: Bargmann W, Möllenstedt G, Niehrs H, Peters D, Ruska E, Wolpers C, editors. Verhandlungen physikalisch-technischer teil. Berlin: Springer Berlin, Heidelberg; 1960. pp. 80-2. DOI
16. Hashimoto H, Kumao A, Eto T, Fujiwara K. Drops of oxides on tungsten oxide needles and nuclei of dendritic crystals. *Journal of Crystal Growth* 1970;7:113-6. DOI
17. Venables JA, Ball DJ, Thomas GJ. An electron microscope liquid helium stage for use with accessories. *J Sci Instrum* 1968;1:121-6. DOI PubMed
18. Bostanjoglo O, Lischke B. Elektronenmikroskopische untersuchungen am kondensierten wasserstoff, stickstoff und sauerstoff. *Zeitschrift für Naturforschung A* 1967;22:1620-2. DOI
19. Honjo G, Kitamura N, Shimaoka K, Mihama K. Low temperature specimen method for electron diffraction and electron microscopy. *J Phys Soc Jpn* 1956;11:527-36. DOI
20. Venables JA. Liquid helium cooled tilting stage for an electron microscope. *Review of Scientific Instruments* 1963;34:582-3. DOI
21. Piercy GR, Gilbert RW, Howe LM. A liquid helium cooled finger for the Siemens electron microscope. *J Sci Instrum* 1963;40:487-9. DOI
22. Goringe MJ, Valdrè U. Use of the bright field shadow technique to study superconductivity in the electron microscope. *Philosophical*

- Magazine* 1963;8:1999-2003. DOI
23. Boersch H, Bostanjoglo O, Niedrig H. Temperaturabhängigkeit der Transparenz dünner Schichten für schnelle Elektronen. *Z Physik* 1964;180:407-14. DOI
  24. Boersch H, Niedrig H, Yersin H. Temperature dependence of large angle electron scattering at polycrystalline gold foils. *Physics Letters A* 1967;25:195-6. DOI
  25. Watanabe H, Ishikawa I. A liquid helium cooled stage for an electron microscope. *Jpn J Appl Phys* 1967;6:83. DOI
  26. Heide HG, Urban K. A novel specimen stage permitting high-resolution electron microscopy at low temperatures. *J Phys E: Sci Instrum* 1972;5:803-8. DOI
  27. Chlebek HG, Curzon AE. A liquid helium stage for the Philips EM 300 electron microscope. *J Phys E: Sci Instrum* 1973;6:1105-6. DOI
  28. Nogales E. The development of cryo-EM into a mainstream structural biology technique. *Nat Methods* 2016;13:24-7. DOI PubMed PMC
  29. Fernández-Morán H. Low-temperature preparation techniques for electron microscopy of biological specimens based on rapid freezing with liquid helium II. *Ann N Y Acad Sci* 1960;85:689-713. DOI PubMed
  30. Taylor KA, Glaeser RM. Electron diffraction of frozen, hydrated protein crystals. *Science* 1974;186:1036-7. DOI PubMed
  31. Chiu W. Electron microscopy of frozen, hydrated biological specimens. *Annu Rev Biophys Biophys Chem* 1986;15:237-57. DOI PubMed
  32. Dubochet J, McDowell A. Vitrification of pure water for electron microscopy. *Journal of Microscopy* 1981;124:3-4. DOI
  33. Dubochet J, Adrian M, Chang JJ, et al. Cryo-electron microscopy of vitrified specimens. *Q Rev Biophys* 1988;21:129-228. DOI PubMed
  34. Adrian M, Dubochet J, Lepault J, McDowell AW. Cryo-electron microscopy of viruses. *Nature* 1984;308:32-6. DOI PubMed
  35. Bostanjoglo O, Röhlke K. Superferromagnetism in thin Gd and Gd-Au films. *Phys Stat Sol (a)* 1971;7:387-92. DOI
  36. Gai P, Gai P. In-situ environmental transmission electron microscopy. In: Kirkland A, Haigh S, Kroto H, O'Brien P, Craighead H, editors. *Nanocharacterisation*. The Royal Society of Chemistry; 2007. pp. 268-90. DOI
  37. Gai PL, Boyes ED. Dynamic *in situ* experiments in a 1 Å double aberration corrected environment. In: Luysberg M, Tillmann K, Weirich T, editors. *EMC 2008 14th European microscopy congress 1-5 September 2008, Aachen, Germany*. Berlin: Springer Berlin Heidelberg; 2008. pp. 479-80. DOI
  38. Kamino T, Saka H. A newly developed high resolution hot stage and its application to materials characterization. *Microsc Microanal Microstruct* 1993;4:127-35. DOI
  39. Gai PL, Boyes ED. Advances in atomic resolution *in situ* environmental transmission electron microscopy and 1 Å aberration corrected *in situ* electron microscopy. *Microsc Res Tech* 2009;72:153-64. DOI PubMed
  40. Tai K, Liu Y, Dillon SJ. *In situ* cryogenic transmission electron microscopy for characterizing the evolution of solidifying water ice in colloidal systems. *Microsc Microanal* 2014;20:330-7. DOI PubMed
  41. Bell D, Zandbergen H. A JEOL-based cooling holder with a low specimen drift allowing sub 1 Å STEM imaging. *European Microscopy Congress 2016: Proceedings*. Wiley; 2016. p. 352-3. DOI
  42. Hotz MT, Corbin G, Dellby N, et al. Optimizing the Nion STEM for *in-situ* experiments. *Microsc Microanal* 2018;24:1132-3. DOI
  43. Goodge BH, Bianco E, Schnitzer N, Zandbergen HW, Kourkoutis LF. Atomic-resolution cryo-STEM across continuously variable temperatures. *Microsc Microanal* 2020;26:439-46. DOI PubMed
  44. Fernandez-Leiro R, Scheres SH. Unravelling biological macromolecules with cryo-electron microscopy. *Nature* 2016;537:339-46. DOI PubMed PMC
  45. Ross FM. Opportunities and challenges in liquid cell electron microscopy. *Science* 2015;350:aaa9886. DOI PubMed
  46. Dubochet J. On the development of electron cryo-microscopy (Nobel lecture). *Angew Chem Int Ed Engl* 2018;57:10842-6. DOI PubMed
  47. Cui Y, Kourkoutis L. Imaging sensitive materials, interfaces, and quantum materials with cryogenic electron microscopy. *Acc Chem Res* 2021;54:3619-20. DOI PubMed
  48. Zachman MJ, Tu Z, Choudhury S, Archer LA, Kourkoutis LF. Cryo-STEM mapping of solid-liquid interfaces and dendrites in lithium-metal batteries. *Nature* 2018;560:345-9. DOI PubMed
  49. Fan Z, Zhang L, Baumann D, et al. *In situ* transmission electron microscopy for energy materials and devices. *Adv Mater* 2019;31:e1900608. DOI PubMed
  50. Liang J, Xiao X, Chou TM, Libera M. Analytical cryo-scanning electron microscopy of hydrated polymers and microgels. *Acc Chem Res* 2021;54:2386-96. DOI PubMed
  51. Gong X, Gnanasekaran K, Chen Z, et al. Insights into the structure and dynamics of metal-organic frameworks via transmission electron microscopy. *J Am Chem Soc* 2020;142:17224-35. DOI PubMed
  52. Li Y, Zhou W, Li Y, et al. Unravelling atomic structure and degradation mechanisms of organic-inorganic halide perovskites by cryo-EM. *Joule* 2019;3:2854-66. DOI PubMed PMC
  53. Hart JL, Cha JJ. Seeing quantum materials with cryogenic transmission electron microscopy. *Nano Lett* 2021;21:5449-52. DOI PubMed
  54. El Baggari I, Savitzky BH, Admasu AS, et al. Nature and evolution of incommensurate charge order in manganites visualized with cryogenic scanning transmission electron microscopy. *Proc Natl Acad Sci U S A* 2018;115:1445-50. DOI PubMed PMC

55. Bianco E, Kourkoutis LF. Atomic-resolution cryogenic scanning transmission electron microscopy for quantum materials. *Acc Chem Res* 2021;54:3277-87. DOI PubMed
56. Jiang T, Ni F, Recalde-benitez O, et al. Observation of dislocation-controlled domain nucleation and domain-wall pinning in single-crystal BaTiO<sub>3</sub>. *Applied Physics Letters* 2023;123:202901. DOI
57. Ignatans R, Damjanovic D, Tileli V. Local hard and soft pinning of 180° domain walls in BaTiO<sub>3</sub> probed by in situ transmission electron microscopy. *Phys Rev Materials* 2020;4:104403. DOI
58. Ignatans R, Damjanovic D, Tileli V. Individual barkhausen pulses of ferroelastic nanodomains. *Phys Rev Lett* 2021;127:167601. DOI PubMed
59. O'Reilly T, Holsgrove K, Arredondo M. Investigating BaTiO<sub>3</sub> via in situ heating TEM. *Microsc. Electron Ion Microsc* 2021. Available from: <https://analyticalscience.wiley.com/content/article-do/investigating-batio3-via-situ-heating-tem> [Last accessed on 21 Sep 2024].
60. O'Reilly T, Holsgrove KM, Zhang X, et al. The effect of chemical environment and temperature on the domain structure of free-standing BaTiO<sub>3</sub> via in situ STEM. *Adv Sci (Weinh)* 2023;10:e2303028. DOI PubMed PMC
61. Tsuda K, Sano R, Tanaka M. Nanoscale local structures of rhombohedral symmetry in the orthorhombic and tetragonal phases of BaTiO<sub>3</sub> studied by convergent-beam electron diffraction. *Phys Rev B* 2012;86:214106. DOI
62. Mun J, Peng W, Roh CJ, et al. In situ cryogenic HAADF-STEM observation of spontaneous transition of ferroelectric polarization domain structures at low temperatures. *Nano Lett* 2021;21:8679-86. DOI PubMed
63. Tyukalova E, Vimal Vas J, Ignatans R, et al. Challenges and applications to *operando* and *in situ* TEM imaging and spectroscopic capabilities in a cryogenic temperature range. *Acc Chem Res* ;2021:3125-35. DOI PubMed
64. Wang YL, He ZB, Damjanovic D, Tagantsev AK, Deng GC, Setter N. Unusual dielectric behavior and domain structure in rhombohedral phase of BaTiO<sub>3</sub> single crystals. *Journal of Applied Physics* 2011;110:014101. DOI
65. Recalde-Benitez O, Pivak Y, Jiang T, et al. Weld-free mounting of lamellae for electrical biasing *operando* TEM. *Ultramicroscopy* 2024;260:113939. DOI PubMed
66. Pivak Y, Sun H, van Omme T, et al. Development of a stable cryogenic in situ biasing system for atomic resolution (s)TEM. *Microsc Microanal* 2023;29:1695. DOI PubMed
67. Omme JT, Zakhosheva M, Spruit RG, Sholkina M, Pérez Garza HH. Advanced microheater for in situ transmission electron microscopy; enabling unexplored analytical studies and extreme spatial stability. *Ultramicroscopy* 2018;192:14-20. DOI PubMed
68. Krisper R, Lammer J, Pivak Y, Fisslthaler E, Grogger W. The performance of EDXS at elevated sample temperatures using a MEMS-based in situ TEM heating system. *Ultramicroscopy* 2022;234:113461. DOI PubMed
69. Yang Y, Vijayan S, Yesibolati MN, Jinschek JR. Standard calibrations and prediction for thermal gradients during in situ transmission electron microscopy heating experiments. *Microscopy and Microanalysis* 2024;30:ozae044.824. DOI
70. Vijayan S, Wang R, Kong Z, Jinschek JR. Quantification of extreme thermal gradients during in situ transmission electron microscope heating experiments. *Microsc Res Tech* 2022;85:1527-37. DOI PubMed
71. Molina-Luna L, Wang S, Pivak Y, et al. Enabling nanoscale flexoelectricity at extreme temperature by tuning cation diffusion. *Nat Commun* 2018;9:4445. DOI PubMed PMC
72. Merz WJ. The electric and optical behavior of BaTiO<sub>3</sub> single-domain crystals. *Phys Rev* 1949;76:1221. DOI
73. Zhuo F, Zhou X, Gao S, et al. Anisotropic dislocation-domain wall interactions in ferroelectrics. *Nat Commun* 2022;13:6676. DOI PubMed PMC
74. Fujii I, Trolrier-mckinsty S. Temperature dependence of dielectric nonlinearity of BaTiO<sub>3</sub> ceramics. *Microstructures* 2023;3. DOI
75. Hershkovitz A, Johann F, Barzilay M, Hendler Avidor A, Ivry Y. Mesoscopic origin of ferroelectric-ferroelectric transition in BaTiO<sub>3</sub>; orthorhombic-to-tetragonal domain evolution. *Acta Materialia* 2020;187:186-90. DOI
76. Zhuo F, Zhou X, Gao S, et al. Intrinsic-strain engineering by dislocation imprint in bulk ferroelectrics. *Phys Rev Lett* 2023;131:016801. DOI PubMed
77. Wu H, Zhu J, Zhang T. Pseudo-first-order phase transition for ultrahigh positive/negative electrocaloric effects in perovskite ferroelectrics. *Nano Energy* 2015;16:419-27. DOI
78. Li YL, Hu SY, Choudhury S, et al. Influence of interfacial dislocations on hysteresis loops of ferroelectric films. *Journal of Applied Physics* 2008;104:104110. DOI
79. Zhang S, Li F, Jiang X, Kim J, Luo J, Geng X. Advantages and challenges of relaxor-PbTiO<sub>3</sub> ferroelectric crystals for electroacoustic transducers - a review. *Prog Mater Sci* 2015;68:1-66. DOI PubMed PMC
80. Marton P, Rychetsky I, Hlinka J. Domain walls of ferroelectric BaTiO<sub>3</sub> within the ginzburg-landau-devonshire phenomenological model. *Phys Rev B* 2010;81:144125. DOI
81. Chou J, Lin M, Lu H. Ferroelectric domains in pressureless-sintered barium titanate. *Acta Materialia* 2000;48:3569-79. DOI
82. Williams DB, Carter CB. Transmission electron microscopy: a textbook for materials science. 2nd ed. Springer; 2008. DOI
83. Höfling M, Zhou X, Riemer LM, et al. Control of polarization in bulk ferroelectrics by mechanical dislocation imprint. *Science* 2021;372:961-4. DOI PubMed
84. Everhardt AS, Damerio S, Zorn JA, et al. Periodicity-doubling cascades: direct observation in ferroelastic materials. *Phys Rev Lett* 2019;123:087603. DOI PubMed
85. Acosta M, Novak N, Rojas V, et al. BaTiO<sub>3</sub>-based piezoelectrics: fundamentals, current status, and perspectives. *Applied Physics Reviews* 2017;4:041305. DOI

86. Qiu C, Wang B, Zhang N, et al. Transparent ferroelectric crystals with ultrahigh piezoelectricity. *Nature* 2020;577:350-4. DOI PubMed
87. Nataf GF, Guennou M, Gregg JM, et al. Domain-wall engineering and topological defects in ferroelectric and ferroelastic materials. *Nat Rev Phys* 2020;2:634-48. DOI
88. Hlinka J, Márton P. Phenomenological model of a 90° domain wall in BaTiO<sub>3</sub>-type ferroelectrics. *Phys Rev B* 2006;74:104104. DOI
89. Erhart J, Cao W. Permissible symmetries of multi-domain configurations in perovskite ferroelectric crystals. *Journal of Applied Physics* 2003;94:3436-45. DOI
90. Gao J, Xue D, Liu W, Zhou C, Ren X. Recent progress on BaTiO<sub>3</sub>-based piezoelectric ceramics for actuator applications. *Actuators* 2017;6:24. DOI
91. Ren X. Large electric-field-induced strain in ferroelectric crystals by point-defect-mediated reversible domain switching. *Nat Mater* 2004;3:91-4. DOI PubMed
92. Zhuo F, Zhou X, Dietrich F, et al. Dislocation density-mediated functionality in single-crystal BaTiO<sub>3</sub>. *Adv Sci (Weinh)* 2024;11:e2403550. DOI PubMed PMC
93. Jiang T, Zhuo F, Recalde-benitez O, Pivak Y, Molina-luna L. Atomic-scale analysis of dislocation-controlled domain nucleation and domain-wall pinning in single-crystal BaTiO<sub>3</sub> by cryo/heating MEMS-based in situ TEM. *Microscopy and Microanalysis* 2024;30:ozae044.675. DOI